Supplementary information

Enhanced western Mediterranean rainfall during past interglacials driven by North Atlantic pressure changes

Yama Dixit[1,2*], Samuel Toucanne[1], Juan M. Lora[4], Christophe Fontanier[5,6,7], Virgil Pasquier[2], Gwenael Jouet[1], Aradhna Tripati[1,2,4]

[1]IFREMER, Laboratoire Géophysique et Enregistrements Sédimentaires, CS10070, 29280 Plouzané cedex, France

[2]Institut Universitaire Européen de la Mer (IUEM), Université de Bretagne Occidentale, Plouzané, France

[3]Department for the Study of Recent and Fossil Bio-Indicators, Angers University, UPRES EA 2644, 2 Boulevard Lavoisier, 49045 Angers Cedex, France

[4] Department of Atmospheric and Oceanic Sciences, Institute of the Environment and Sustainability, Department of Earth, Planetary, and Space Sciences, University of California, Los Angeles, USA

[5]EPOC UMR 5805, Université de Bordeaux, Pessac, France

[6]FORAM, Study group, Villevêque, France

[7]Université d'Angers, Angers, France

Supplementary text

Lake level and cave records from the Northern Mediterranean borderlands

The following records are shown in Figure 4 of the main text. The numbers denote sites with data constraining hydroclimate changes including from this work (blue star) and high rainfall/ high lake levels (blue circles) that are consistent with high winter precipitation during the early-middle Holocene. Dark blue lined circles are records covering all the three interglacials including the Holocene interglacial, the last interglacial, and the penultimate interglacial. Red circles denote the lakes with lower lake levels during the Holocene. (1) Lake Medina in southern Spain (Reed et al., 2001); (2) Lake Siles in southern Spain (Carrión, 2002); (3) Lake Cerin (Magny et al., 2011); (4) Lake Ledro in northern Italy (Magny et al., 2012); (5) Lake Accesa in central Italy (Magny et al., 2007); (6) Corchia Cave (Drysdale et al., 2005); (7) Lake Grande diMonticchio in Basilicata, southern Italy (Allen et al., 1999); (8) Lake Albano and Lake Nema (Ariztegui et al., 2000); (9) Lake Preola in Sicily (Magny et al., 2011); (10) Lake Xinias in northern Greece (Digerfeldt et al., 2007); (11) Boras Mountains in northern Greece (Lawson et al., 2005); (12) Tenaghi Philippon in northern Greece (Tzedakis, 2007); (13) Lake Golhisar in south-western Turkey (Eastwood et al., 2007); (14) Lake Eski Acigol in central Turkey (Turner et al., 2008); (15) Lake Van in Turkey (Pickarski and Litt, 2017).

MIS 7 temperature mystery

MIS 7c and 7e are observed as warmer than present interstadials globally. However, our record from Northern Tyrhennian Sea shows colder temperatures during MIS 7c. The Mg/Ca-SSTs closely follow the runoff proxy, Ba/Ca values. The close correspondence in the evolution of Ba/Ca ratios and Mg/Ca-SST suggest the temperatures recorded in sediment core GDEC-4-2 during this period were in fact caused by the plume of cold fresh water of the Golo River at this site (Fig. S4). This is in contrast to MIS5e when the site was not bathed in river water and SSTs reflects atmospheric temperatures (Fig. 2).

First order estimation of Sea Surface Salinity (SSS) from foraminifera Ba/Ca

We collected five water samples from sites off of the Golo River starting from its mouth to the open sea in an attempt to quantify past sea surface salinity (Table S3). Ba/Ca in plantonic foraminifer is calculated from Ba/Ca (umol/mol) in sea water using the partition coefficient of $D_{Ba} = 0.147$, where $Ba/Ca_{seawater} * D_{Ba} = Ba/Ca_{foram}$ (Lea and Spero, 1994). Owing to limited paired measurements of modern salinity and Ba from sites of the modern Golo River, we only present a semi-quantitative first order estimates of past sea surface salinity (SSS) (Fig. S5). We estimate past SSS using variation of planktonic foraminiferal Ba/Ca and the modern SSS-Ba/Ca relationship, as previously demonstrated by Weldeab et al., (2007) for Congo River. $Ba/Ca_{seawater}$ is obtained using the measured Ba and the corresponding Ca has been calculated assuming a conservative behaviour of Ca and a linear relationship of Ca with salinity that is, a salinity of 35 corresponds to 10.2 mmol/kg (Weldeab et al., 2007). The relationship between SSS and Ba/Ca in seawater from three large tropical

rivers Congo, Amazon, and Ganges-Brahmaputra has been previously demonstrated (Weldeab et al., 2007). SSS estimates are shown in Fig. S6.

Table S1: PMIP3 models used in this study.

Model	**Institute**
BCC-CSM1-1	Beijing Climate Center, China Meteorological Administration
CCSM4	National Center for Atmospheric Research
CNRM-CM5	Centre National de Recherches Mete orologiques/Centre Europeen de Recherche et de Formation Avancee en Calcul Scientifique
CSIRO-Mk3-6-0	Commonwealth Scientific and Industrial Research Organisation
CSIRO-Mk3L-1-2	Commonwealth Scientific and Industrial Research Organisation
FGOALS-g2	Institute of Atmospheric Physics, Chinese Academy of Sciences, and Tsinghua University
FGOALS-s2	Institute of Atmospheric Physics, Chinese Academy of Sciences, and Tsinghua University
GISS-E2-R_p150	NASA Goddard Institute for Space Studies
IPSL-CM5A-LR	Institut Pierre-Simon Laplace
MIROC-ESM	Japan Agency for Marine-Earth Science and Technology, Atmosphere and Ocean Research Institute (University of Tokyo), National Institute for Environmental Studies
MPI-ESM-P_p1	Max Planck Institute for Meteorology
MRI-CGCM3	Meteorological Research Institute

Table S2: Chronology for the last glacial termination showing corresponding tie-points in GDEC 4-2 core used in this study and ODP 975.

GDEC-4-2 depth (mbsf)	ODP975 age (ka; Marino et al., 2015)
33.98	111.30
34.1	118.78
35.45	125.15
36.65	127.61
37	128.94
37.77	131.79
39.7	134.85
44.3	146.50

Table S3: Locations of sites from where water samples were collected off the Golo River in March 2017. Also shown are the corresponding surface and deep-water salinity values taken at the time of water collection.

Location		Latitude and longitude	Salinity		Calculated $Ba/Ca_{seawater}$
			Surface	Deep	μmol/mol
Station 1	42.52591°N	9.52927°E	0.86	0.86	2146.354
Station 2	42.52508°N	9.53178°E	1.21	1.30	354.143
Station 3	42.52536°N	9.53513°E	4.26	20.24	188.532
Station 4	42.52401°N	9.53646°E	38.24	38.31	5.969
Station 5	42.52497°N	9.53874°E	38.16	38.18	5.924

Supplementary Figure S1

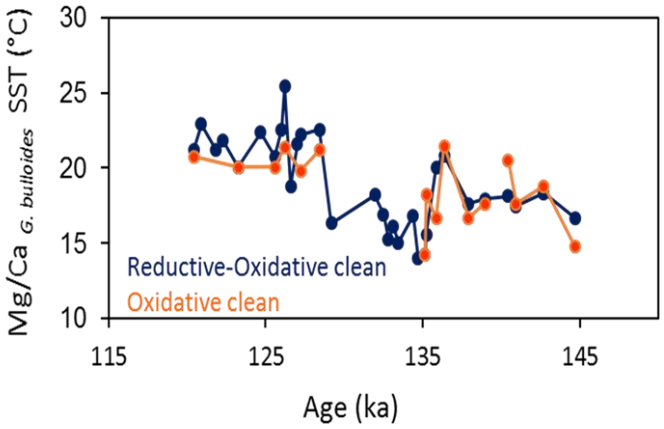

Figure S1. Impact of chemical cleaning procedure on Mg/Ca-based SST. Mg/Ca temperatures calculated on oxidatively cleaned *G. bulloides* (orange) and using both reductive-oxidative (Boyle and Rosenthal, 1996) and oxidative only (Barker et al., 2003) cleaning procedures shown in blue. Choice of cleaning method does not alter the reconstructed Mg/Ca- SSTs.

Supplementary Figure S2

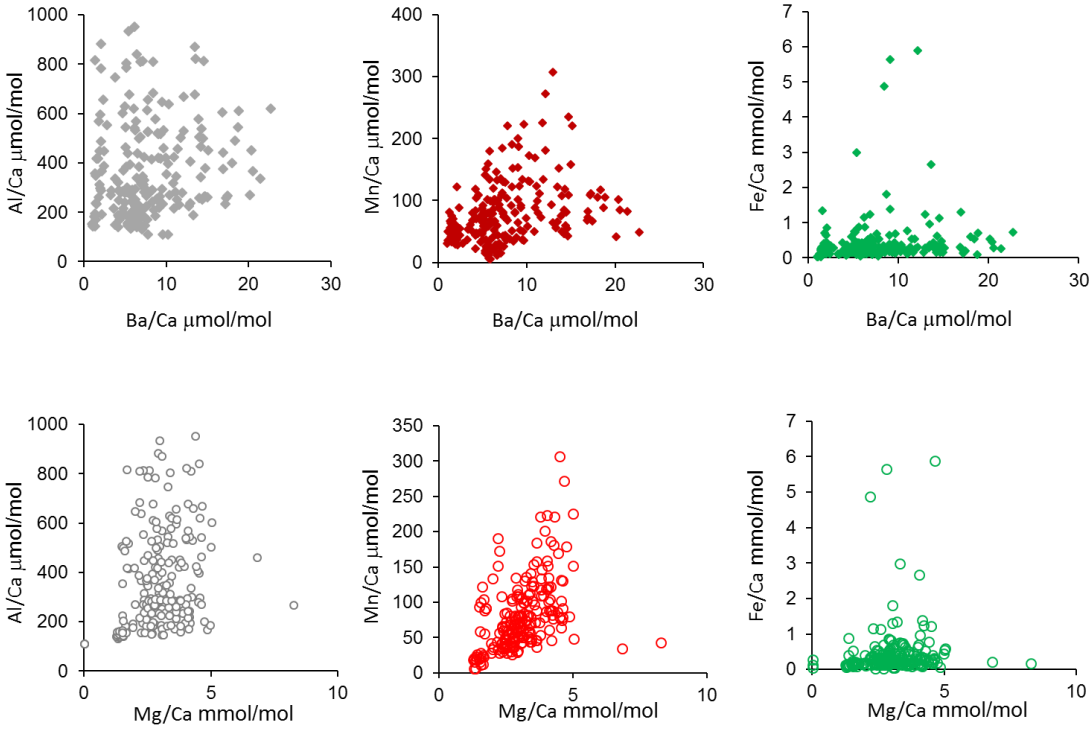

Figure S2. Indicators of contamination in reductively cleaned planktic foraminiferal test samples. Mn/Ca, Al/Ca and Fe/Ca ratios versus Ba/Ca and Mg/Ca ratios obtained from the reductively cleaned test samples of *G. bulloides.* The Mn/Ca, Al/Ca and Fe/Ca ratios show no correlation with the Ba/Ca and Mg/Ca values indicating that phases contributing to elevated Mn/Ca, Al/Ca and Fe/Ca ratios are not impacting Ba/Ca and Mg/Ca. This approach has been utilized to assess if foraminiferal elemental proxies are impacted by the presence of contaminants (e.g., Skinner et al., 2003; Barker et al., 2003; Doss and Marchitto, 2013).

Supplementary Figure S3

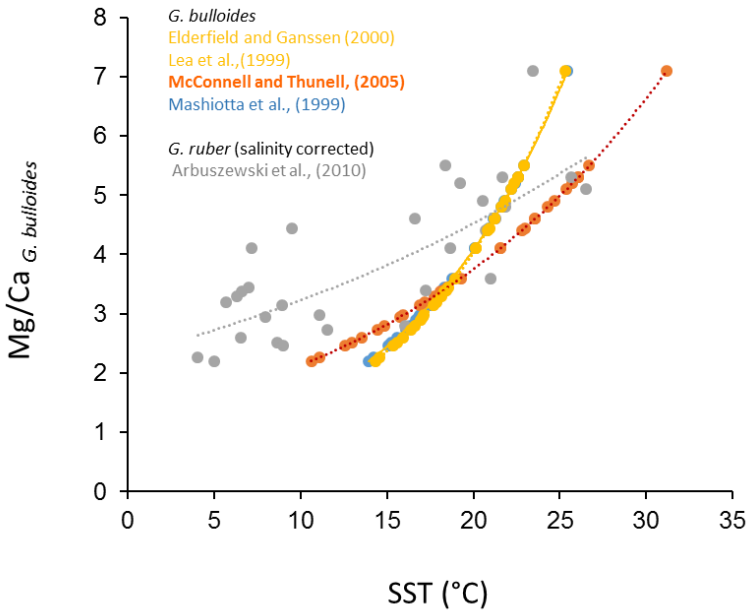

Figure S3. Available Mg/Ca to Sea surface temperature (SSTs) calibration equations for *G. bulloides.* Since the SSTs calculated using McConnell and Thunell (2005) calibration for *G. bulloides* is applicable for temperatures ranging from 16 to 33°C, we used the McConnell and Thunell calibration for SST determination.

Supplementary Figure S4

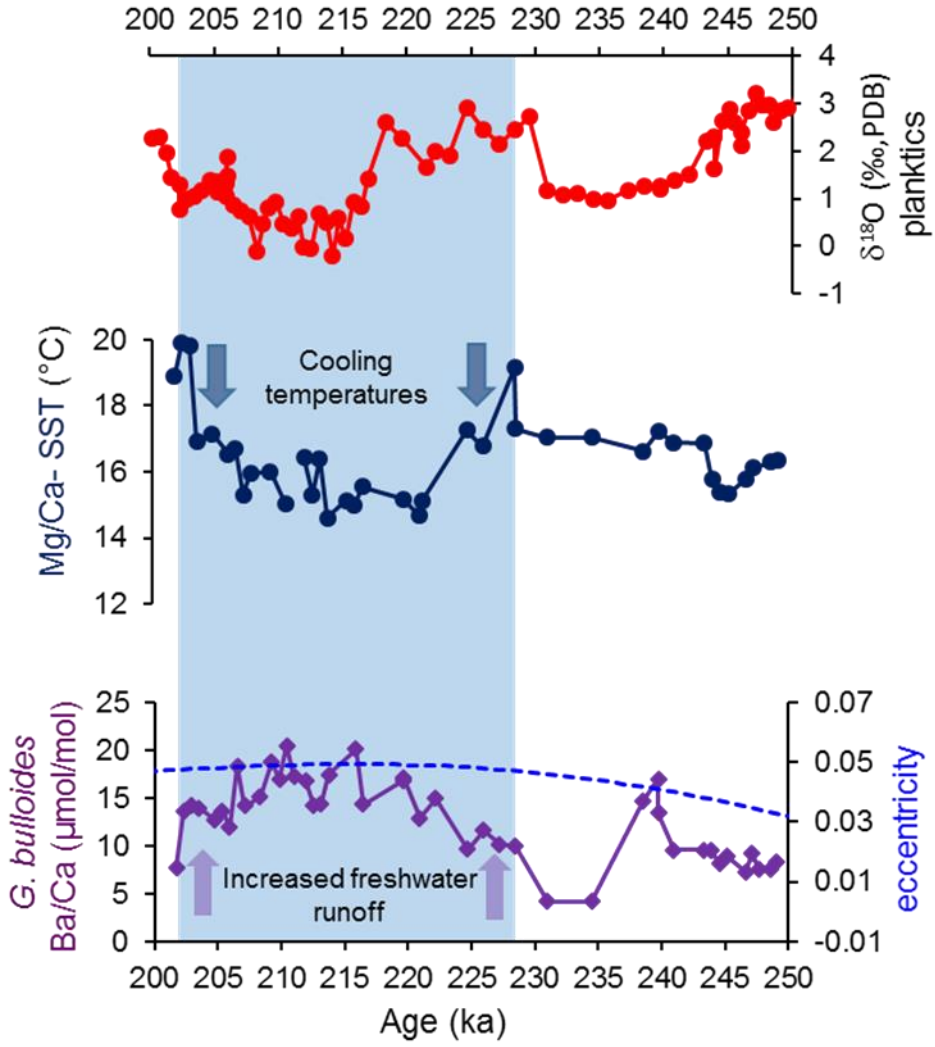

Figure S4: Elevated Ba/Ca ratios lead Mg/Ca-SST decline, indicating reduced salinity occurred before cooling during warm interglacial MIS 7c. The close correspondence in the evolution of Ba/Ca ratios and Mg/Ca-SST suggest the temperatures recorded in sediment core GDEC-4-2 during this period were in fact caused by the plume of cold fresh water of the Golo River at this site.

Supplementary Figure S5

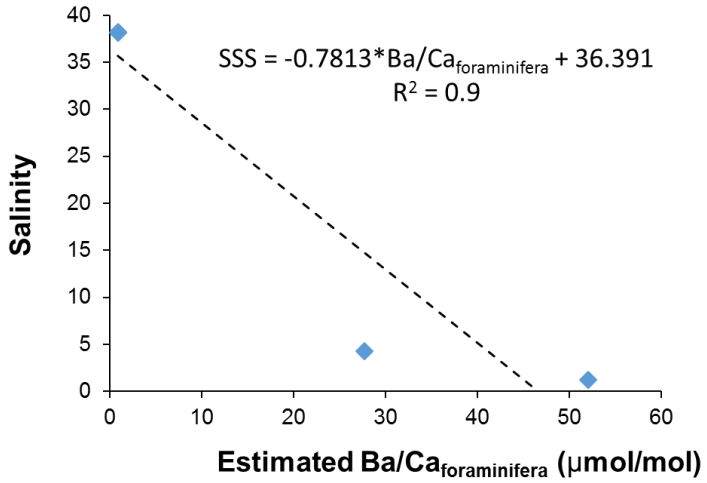

Figure S5. Past sea surface salinity (SSS) is estimated using variation of planktonic foraminiferal Ba/Ca calculated from measured values of Ba/Ca of seawater and the modern SSS-Ba/Ca relationship (see inset in Figure).

Supplementary Figure 6

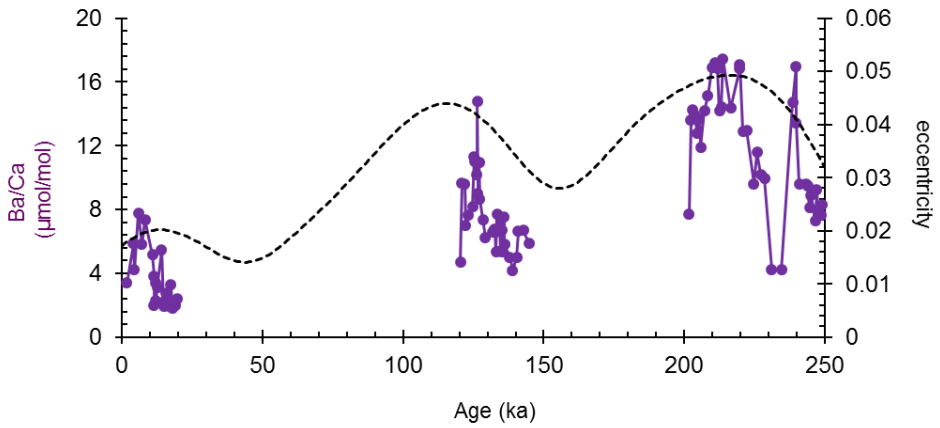

Figure S6. Change in the amplitude of Ba/Ca follows the eccentricity cycle, with higher Ba/Ca during MIS-7, relatively lower Ba/Ca in MIS-5, and the lowest Ba/Ca in MIS-1, corresponding to the respective insolation maxima of the 100 ka-eccentricity cycle during each interglacial. This trend in the change in magnitude of river discharge due to winter rainfall confirms the idea of eccentricity modulation of the precession-driven rainfall/runoff in the Mediterranean during the late Pleistocene,

Supplementary Figure 7

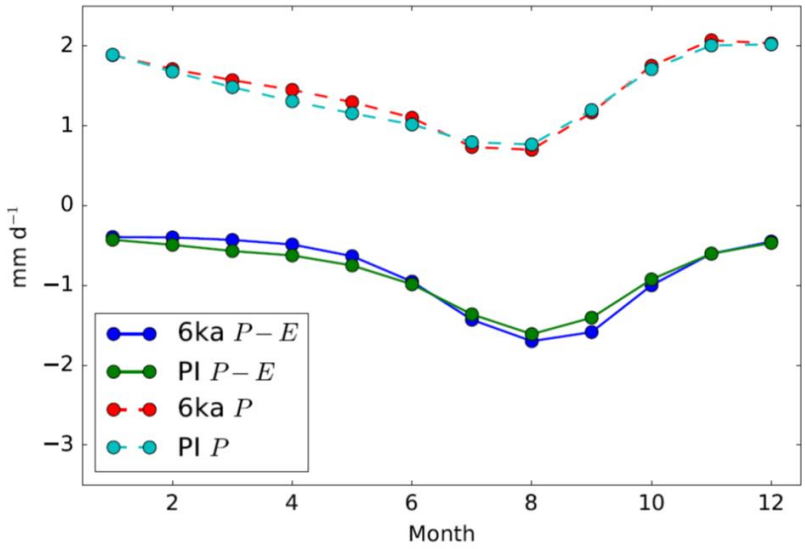

Figure S7. Time series plot showing high seasonality in Precipitation (*P*) and Precipitation- Evaporation (*P* – *E*). Notice that the models show that the biggest change happens in January-May, and this is because there is a strengthened seasonality in *P* and *P* – *E*. There is more late-winter moisture in the Mediterranean, and less summertime moisture.

Supplementary Figure 8

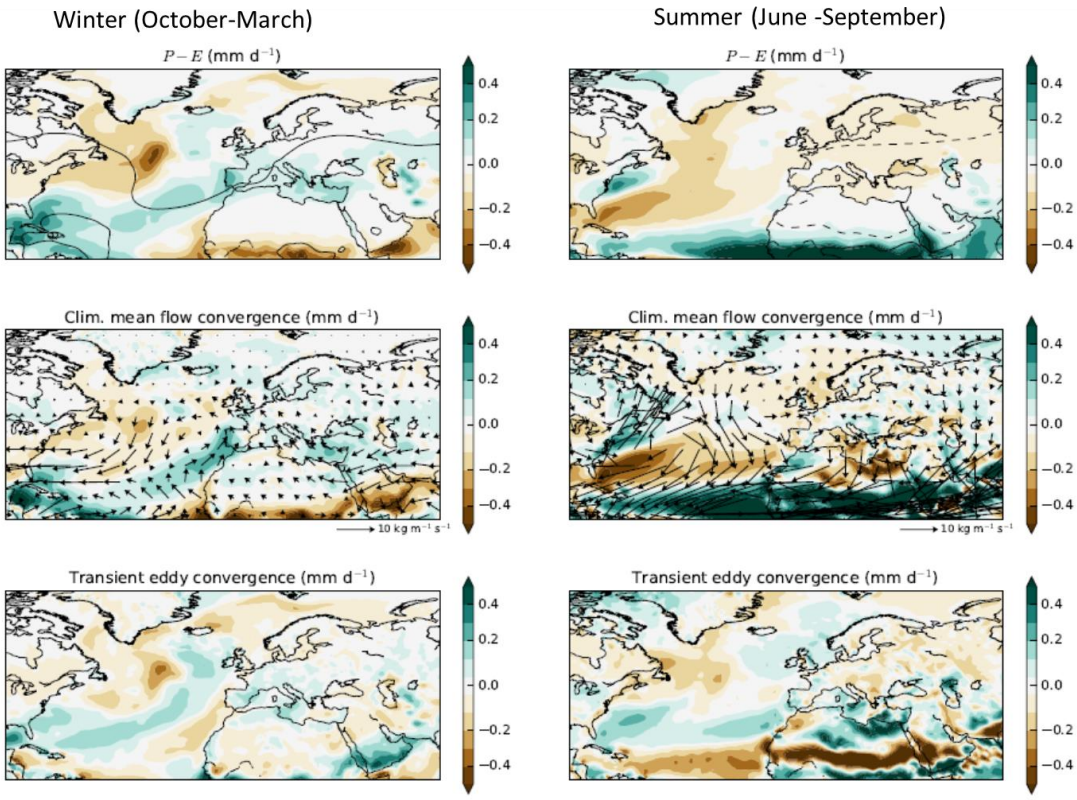

Figure S8. Difference between Holocene – pre-industrial PMIP3 multi-model ensemble means for winter and summer. The top panel (colored contours) show the change in winter (October to March) and summer (April to September) precipitation minus evaporation (*P* – *E*) between the mid-Holocene and pre-industrial periods, and represents to mean of 11 PMIP3 models (Braconnot et al., 2012). The second panel show the corresponding differences in mean moisture transport for the region (arrows). Note the increased southwesterly mean moisture transport into the western Mediterranean, as well as decreased westerly transport (shown by easterly arrows) across the eastern Mediterranean as well as the northern North Atlantic during winter season. The considerable increases in moisture transport due to the African monsoon are also visible.

References:

Allen, J.R.M., Brandt, U., Brauer, A., Hubberten, H.-W., Huntley, B., Keller, J., Kraml, M., Mackensen, A., Mingram, J., Negendank, J.F.W., 1999. Rapid environmental changes in southern Europe during the last glacial period. Nature 400, 740–743.

Ariztegui, D., Asioli, A., Lowe, J.J., Trincardi, F., Vigliotti, L., Tamburini, F., Chondrogianni, C., Accorsi, C.A., Bandini Mazzanti, M., Mercuri, A.M., Van der Kaars, S., McKenzie, J.A., Oldfield, F., 2000. Palaeoclimate and the formation of sapropel S1: inferences from Late Quaternary lacustrine and marine sequences in the central Mediterranean region. Palaeogeogr. Palaeoclimatol. Palaeoecol. 158, 215–240. https://doi.org/10.1016/S0031-0182(00)00051-1

Barker, S., Greaves, M., Elderfield, H., 2003. A study of cleaning procedures used for foraminiferal Mg/Ca paleothermometry. Geochemistry, Geophys. Geosystems 4.

Boyle, E., Rosenthal, Y., 1996. Chemical hydrography of the South Atlantic during the last glacial maximum: Cd vs. δ13C, in: The South Atlantic. Springer, pp. 423–443.

Braconnot, P., Harrison, S.P., Kageyama, M., Bartlein, P.J., Masson-Delmotte, V., Abe-Ouchi, A., Otto-Bliesner, B., Zhao, Y., 2012. Evaluation of climate models using palaeoclimatic data. Nat. Clim. Chang. 2, 417.

Carrión, J.S., 2002. Patterns and processes of Late Quaternary environmental change in a montane region of southwestern Europe. Quat. Sci. Rev. 21, 2047–2066. https://doi.org/10.1016/S0277-3791(02)00010-0

Digerfeldt, G., Sandgren, P., Olsson, S., 2007. Reconstruction of Holocene lake-level changes in Lake Xinias, central Greece. The Holocene 17, 361–367.

Doss, W., Marchitto, T.M., 2013. Glacial deep ocean sequestration of CO 2 driven by the eastern equatorial Pacific biologic pump. Earth Planet. Sci. Lett. 377, 43–54.

Drysdale, R.N., Zanchetta, G., Hellstrom, J.C., Fallick, A.E., Zhao, J., 2005. Stalagmite evidence for the onset of the Last Interglacial in southern Europe at 129 ± 1 ka. Geophys. Res. Lett. 32, n/a-n/a. https://doi.org/10.1029/2005GL024658

Eastwood, W.J., Leng, M.J., Roberts, N., Davis, B., 2007. Holocene climate change in the eastern Mediterranean region: a comparison of stable isotope and pollen data from Lake Gölhisar, southwest Turkey. J. Quat. Sci. 22, 327–341.

Lawson, I.T., Al-Omari, S., Tzedakis, P.C., Bryant, C.L., Christaniss, K., 2005. Lateglacial and Holocene vegetation history at Nisi Fen and the Boras mountains, northern Greece. The Holocene 15, 873–887.

Lea, D.W., Spero, H.J., 1994. Assessing the reliability of paleochemical tracers: Barium uptake in the shells of planktonic foraminifera. Paleoceanography 9,

445–452. https://doi.org/10.1029/94PA00151

Magny, M., Bossuet, G., Ruffaldi, P., Leroux, A., Mouthon, J., 2011. Orbital imprint on Holocene palaeohydrological variations in west-central Europe as reflected by lake-level changes at Cerin (Jura Mountains, eastern France). J. Quat. Sci. 26, 171–177.

Magny, M., De Beaulieu, J.-L., Drescher-Schneider, R., Vannière, B., Walter-Simonnet, A.-V., Miras, Y., Millet, L., Bossuet, G., Peyron, O., Brugiapaglia, E., 2007. Holocene climate changes in the central Mediterranean as recorded by lake-level fluctuations at Lake Accesa (Tuscany, Italy). Quat. Sci. Rev. 26, 1736–1758.

Magny, M., Joannin, S., Galop, D., Vannière, B., Haas, J.N., Bassetti, M., Bellintani, P., Scandolari, R., Desmet, M., 2012. Holocene palaeohydrological changes in the northern Mediterranean borderlands as reflected by the lake-level record of Lake Ledro, northeastern Italy. Quat. Res. 77, 382–396.

Pickarski, N., Litt, T., 2017. A new high-resolution pollen sequence at Lake Van, Turkey: insights into penultimate interglacial–glacial climate change on vegetation history. Clim. Past 13, 689.

Reed, J.M., Stevenson, A.C., Juggins, S., 2001. A multi-proxy record of Holocene climatic change in southwestern Spain: the Laguna de Medina, Cádiz. The Holocene 11, 707–719.

Skinner, L.C., Shackleton, N.J., Elderfield, H., 2003. Millennial-scale variability of deep-water temperature and δ18Odw indicating deep-water source variations in the Northeast Atlantic, 0–34 cal. ka BP. Geochemistry, Geophys. Geosystems 4, n/a-n/a. https://doi.org/10.1029/2003GC000585

Toucanne, S., Minto'o, C.M.A., Fontanier, C., Bassetti, M.-A., Jorry, S.J., Jouet, G., 2015. Tracking rainfall in the northern Mediterranean borderlands during sapropel deposition. Quat. Sci. Rev. 129, 178–195.

Turner, R., Roberts, N., Jones, M.D., 2008. Climatic pacing of Mediterranean fire histories from lake sedimentary microcharcoal. Glob. Planet. Change 63, 317–324.

Tzedakis, P.C., 2007. Seven ambiguities in the Mediterranean palaeoenvironmental narrative. Quat. Sci. Rev. 26, 2042–2066.

Weldeab, S., Lea, D.W., Schneider, R.R., Andersen, N., 2007. 155,000 years of West African monsoon and ocean thermal evolution. Science (80-.). 316, 1303–1307.